Structure and physical properties of $Eu_{0.8}Y_{0.2}MnO_3$ ceramics

J. Agostinho Moreira · A. Almeida · W. S. Ferreira ·
M. R. Chaves · J. B. Oliveira · J. M. Machado da Silva ·
M. A. Sá · S. M. F. Vilela · P. B. Tavares

Abstract This work is addressed to study the crystal structure and morphology, as well as the thermodynamic, dielectric and magnetic properties of $Eu_{0.8}Y_{0.2}MnO_3$ ceramics, synthesized by urea sol-gel combustion method. The experimental results were systematically compared with data available for the corresponding single crystals. Though the effect of the anisotropy on both dielectric and magnetic properties is missing, they enabled us to investigate the main physical mechanisms associated with their magnetoelectric properties, in particular the one which drives the ferroelectric phase. The phase sequence and critical temperatures are in good agreement with the corresponding values reported for single crystals. Similarly, structural results evidence strong distortions of the crystal lattice, enhancing the ferromagnetic interactions over the antiferomagnetic ones. A significant contribution of the magnetic fluctuations above T_N was also evidenced from the magnetization studies.

J. A. Moreira (✉) · A. Almeida · W. S. Ferreira · M. R. Chaves ·
J. B. Oliveira · J. M. M. da Silva · M. A. Sá
IFIMUP and IN- Institute of Nanoscience and Nanotechnology,
Departamento de Física e Astronomia da Faculdade de Ciências
da Universidade do Porto,
Rua do Campo Alegre, 687,
4169-007 Porto, Portugal
e-mail: jamoreir@fc.up.pt

S. M. F. Vilela · P. B. Tavares
Centro de Química,
Universidade de Trás-os-Montes e Alto Douro,
Apartado 1013,
5001-801 Vila Real, Portugal

PACS classification codes 81.20.Ev · 75.80.+q · 75.40. Cx · 77.22. Gm

1 Introduction

The control of the electric (magnetic) properties by using magnetic (electric) fields has been an interesting issue of research in both physics and materials science for the last decade. The control of the polarization by applied magnetic fields, which is known as the magnetoelectric effect, may emerge in those materials whenever the electric polarization and magnetic orders are coupled to each other [1]. It is worth to note that the concept of magnetoelectric effect does not impose any particular magnetic or dipolar structure of the material, whenever it is observed [1]. In a very special class of materials, called magnetoelectric multiferroics, the magnetoelectric effect can emerge from the coupling between spontaneous polar and magnetic orders of ferroic type, coexisting in the same single phase [1, 2]. Attractive though, such materials are very scarce, and the magnetoelectric effect occurs usually at rather low temperatures. In a few cases, it emerges, however at room temperature, but its strength remains still small [1, 3].

Among the most studied magnetoelectric materials, the undoped perovskite-related rare-earth manganites, with general formula $RMnO_3$, have drawn a lot of scientific interest due to their rich phase diagram, which has been attributed to both the rare-earth ionic radius, and magnetic moment [4–6]. In fact, a strong dependence of the magnetic modulation on the ionic radius (r_R) of the rare-earth ion has been evidenced in earlier works. The ionic radius in $RMnO_3$ also determines the φ=Mn-O-Mn bond angle, which decreases with decreasing r_R. The decrease of φ

suppresses the layer-type antiferromagnetic order among the Mn spins, as it was observed for $NdMnO_3$ and $SmMnO_3$ [4]. Sinusoidal antiferromagnetic order appears at intermediate values of φ ($EuMnO_3$, $GdMnO_3$, $TbMnO_3$ and $DyMnO_3$). For $TbMnO_3$ and $DyMnO_3$, a quite significant magnetoelectric effect has been observed in the long wavelength modulated antiferromagnetic phases [4, 7]. In this scenario, a φ dependence of the super-exchange interaction between nearest neighbour (NN) and next-nearest neighbour Mn sites is expected, and so, the emerging ferroelectricity can be well described in the framework of the inverse Dzyaloshinskii-Morya model [8–10].

Usually, a detailed analysis of the experimental data is rather complex, because it must account for the interplay between the spins of Mn^{3+} and rare-earth ions. Contrarily, the orthorhombic Y-doped $EuMnO_3$ system is a far more easily magnetic system, stemming only from the Mn^{3+} ions. So, the changes of its physical properties due to controlled Y-doping cannot be attributed to additional magnetic moments. $Eu_{0.8}Y_{0.2}MnO3$ is one of the most interesting compositions, as it exhibits both ferroelectric polarization and ferromagnetic properties at low temperatures [11–13]. The paramagnetic phase of $Eu_{0.8}Y_{0.2}MnO_3$ transforms into an antiferromagnetic (AFM-1) phase at T_N=48 K, with an incommensurate sinusoidal collinear arrangement of the Mn^{3+} spins [11, 13]. The anomalies observed in both specific heat and dielectric permittivity hint for another phase transition at T_{AFM-2}=30 K [11, 13]. Double magnetic hysteresis loops at 25 K were reported, revealing the antiferromagnetic character of the phase below T_{AFM-2}, hereafter called AFM-2 [11]. Based on the anomalous behaviour of the magnetization curves, a canted antiferro-magnetic phase (AFM-3) is established below T_{AFM-3}= 25 K [11]. However, the magnetic structure of the low temperature phases remains still unknown.

The phase diagram of $Eu_{0.8}Y_{0.2}MnO_3$ is still a matter of controversy. While Hemberger et al [11] have reported three magnetic phases below T_N, being the two antiferro-magnetic phases below T_{AFM-2} both ferroelectric, Yamasaki et al[13] have found only two magnetic phases for $T<T_N$, and these authors have not observed any kind of ferroelec-tricity in this compound. According to Yamasaki et al[13], the origin of the weak ferromagnetism in $Eu_{0.8}Y_{0.2}MnO_3$ below T_{AFM-3} is likely due to a spin-canting of the A-type antiferromagnetic structure, which prevents the occurrence of ferroelectricity. More recently, a detailed experimental study of the polar properties and magnetoelectric effect in $Eu_{0.8}Y_{0.2}MnO_3$ has corroborated the magnetic phase sequence proposed by Hemberger et al[11], but only the AFM-2 phase is ferroelectric [14].

Most of the experimental work published in this system has been performed in single crystals, which has required the processing of high quality single crystals, using the floating zone method. Currently, much more accessible methods for processing polycrystalline samples are much accessible and cheaper, yielding high quality. Particularly, the sol-gel technique has been proved very adequate for processing rare-earth manganites ceramics.

In this work, we report a detailed study of the crystal structure, specific heat, dielectric constant, and the induced molar magnetization as a function of temperature, in $Eu_{0.8}Y_{0.2}MnO_3$ high quality ceramics, prepared by the urea sol-gel combustion method. Particular attention will be given to both crystal distortions, and thermodynamic properties of the low temperature magnetic phases. The experimental results will be discussed, and compared with those obtained from the corresponding single crystals.

2 Experimental details

The samples were prepared using the urea sol-gel combustion method. Stoichiometric amounts of Eu_2O_3 (Alfa Aesar, chemical purity>99.99%), Y_2O_3 (Aldrich, 99.99%), and $Mn(NO_3)_2 \cdot 4H_2O$ (ABCR chemical purity> 98%) were dissolved in diluted aqueous solution of nitric acid. The pH of the solution was adjusted to 5.2 with diluted ammonia. The added amount of urea was calculated so that 3 moles of urea were presented for each mole of cationic element (Eu + Mn). The solution was then stirred and heated to evaporate all water and decompose the urea. At the end of the process, when the temperature reaches 200ºC, the gel auto ignites and a controlled but fast combustion (3 to 5 s) occurs, yielding a dark powder. This powder was calcinated at 700ºC for 10 h, grounded with a mortar and a pestle, passed through a 38 µm sieve and pelletized. The pellet was thermal treated at 900ºC for 20 h regrounded with a mortar and a pestle, repelletized and treated at 1100ºC for 20 h. Then, the sample was regrounded, repelletized (2 cm diameter) and sintered at 1300ºC for 40 h. The samples were cooled very fast (to 500ºC in less than 20 s), in order to preserve the high temperature equilibrium oxygen ($\delta \approx 0$ in $Eu_{0.8}Y_{0.2}MnO_{3+\delta}$), and in this way, avoid the Mn(IV) ion in the cystal [15]. X-ray diffraction experiments were performed in a PANalytical X'Pert Pro difractometer, equipped with X'Celerator detector and secondary mono-cromator, in $\theta/2\theta$ Bragg-Bentano geometry, at room temperature. The structure was refined by Rietveld model using PowderCell[16] and Rietica[17] software.

The density of the material was determined assuming a perfect cylindrical shape of the pellet, weighting and measuring the dimensions with a vernir callipers. The mass of the pellet was determined using a balance with precision 0.001 g.

The heat capacity was measured in an ARS Cryocooler, between 10 K and 70 K, in a quasi-adiabatic way by means of an impulse heating technique.

The samples used to perform the dielectric measurements have the shape of a regular parallelepiped, provided with gold electrodes. The complex dielectric constant was measured with an HP4284A impedance analyzer, in the 5 K – 300 K temperature range, under an ac electric field of amplitude 1 V/cm for 10 KHz and 1 MHz.

Low-field dc (20-40 Oe) induced specific magnetization measurements, and the magnetic field dependence of the magnetization (M(H)) were carried out using commercial superconducting quantum interference SQUID magnetometer in the temperature range 4 K–300 K.

More details of the experimental techniques and data analysis have been described earlier [18–21].

3 Experimental results and discussion

3.1 Structural study

The valence of the europium ion was checked through XPS technique, and no evidences of the existence of other valences than the Eu (III) could be detected. As the samples were fast cooled from 1350ºC down to room temperature, significant deviations of the oxygen occupancy from the expected stoichiometric $Eu_{0.8}Y_{0.2}MnO_3$ are not expected, excluding the existence of significant amount of Mn (IV) ion [15].

Figure 1 depicts the experimental data and the calculated x-ray diffraction spectrum of $Eu_{0.8}Y_{0.2}MnO_3$, at room temperature. In the same figure it is also shown the difference between both experimental and calculated spectra. No secondary crystallographic phases were detected. By using the density calculated from the x-ray data, which is 6.941 gcm^{-3}, and the actual density of the material 7.056 gcm^{-3}, a compacity of 98% is obtained.

The crystal structrure of $Eu_{0.8}Y_{0.2}MnO_3$ is described by the space group Pbnm, with four formula units per unit cell. The lattice parameters, the atomic positions, and the R-factors, obtained from the Rietveld refinements, are displayed in Table I. The lattice parameters fulfil the $c/\sqrt{2} < a < b$ relation, which is characteristic of the so-called O' structure, typically found in other rare-earth manganites presenting distortions of the octahedral environment of the Mn^{3+} ions, associated with a strong Jahn-Teller distortion of the MnO_6 units and orbital ordering [22, 23]. The tolerance factor is $t = 0.870$. As it will be ascertained in the following, undoped $EuMnO_3$ exhibits already lattice distortions, which are further enhanced by increasing Y-doping.

From Rietveld refinement of the atomic positions, we have calculated the values of both the length and angle of chemical bonds involved in the MnO_6 octahedra, and the Eu/Y-O distances, which are presented in Table II. Figures 2 (a) and (b) show the projections of the unit cell on the *ac*-plane and *ab*-plane. In these figures, the Mn-O bond lengths and Mn-O-Mn bond angles are also indicated.

The crystal structure is formed by a network of corner-sharing MnO_6 octahedra developing zig-zag chains along the *c*-axis. The Eu^{3+} or Y^{3+} ions occupy the interstices between octahedra.

Similar to other orthorhombic rare-earth manganites, three different Mn-O lengths are detected [23]. The difference between the larger and the smaller ones is about 0.3907Å, evidencing a significant distortion of the MnO_6 octahedra. The tilt angle [180°-(Mn-O1-Mn)]/2 is 19.0°, which is about 2.6°, 2.1° and 1.7° larger than the ones observed for $EuMnO_3$, $GdMnO_3$ and $DyMnO_3$, respectively [4]. In order to correlate the angle Mn-O1-Mn, hereafter designated by φ, with the A-site radius (r_R) we have also

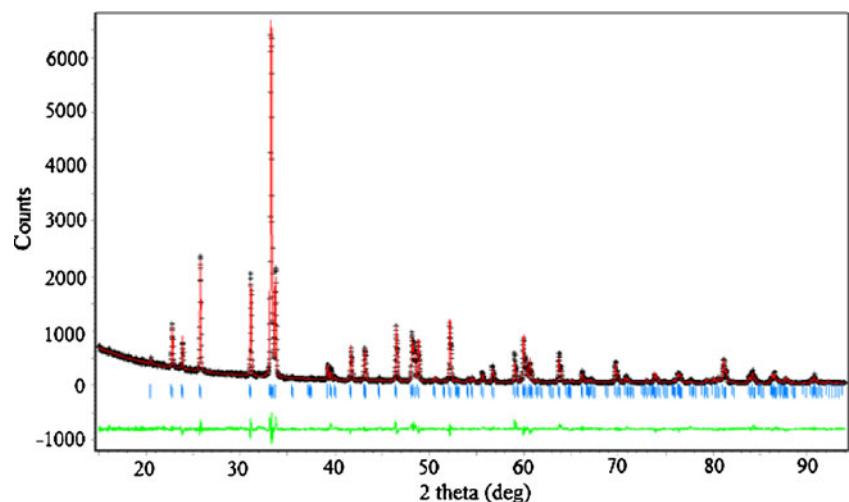Fig. 1 Observed, calculated and difference XRD patterns for the $Eu_{0.8}Y_{0.2}MnO_3$ sample at room temperature

Table I Lattice parameters, atomic positions, and R-factors for $Eu_{0.8}Y_{0.2}MnO_3$ obtained by Rietveld refinement of the x-ray diffraction spectrum pattern at room temperature, using software Rietica [16].

Cell (Å)	Site	Wyckoff Position	x	y	z	B ($Å^2$)
a=5.8561	Eu/Y	$4c$	0.07956	0.25	0.9823	0
b=7.4354	Mn	$4b$	0	0	0.5	0
c=5.3246	O1	$4c$	0.46653	0.25	0.11459	2.585
V=228.06$Å^3$	O2	$8d$	0.16802	0.53607	0.20767	0

R-factors (%): R_p=11.691; R_{wp}=15.622; χ^2=2.734
Overall thermal=0.2168

studied the crystal structure of other orthorhombic rare-earth manganites, processed using the same chemical route, by using the powder x-ray diffraction technique. As it was referred to above, there is a clear connection between both magnetic properties and phase sequence of these compounds, and r_R or φ [4]. Figure 3 shows the φ angle as a function of the ionic radius of the A-site ion, for the $RMnO_3$, with R = Nd, Sm, Eu, Gd, Dy, and for $Eu_{0.8}Y_{0.2}MnO_3$. From Fig. 3 follows that for undoped rare-earth manganites, φ decreases almost linearly as r_R decreases, which is expected to decrease the antiferromagnetic interactions relatively to the ferromagnetic ones [24]. However, for the $Eu_{0.8}Y_{0.2}MnO_3$, a significant deviation from the linear behaviour observed for undoped manganites, is detected. In fact, a slightly decrease of the effective A-site radius, due to the partial substitution of Eu^{3+} ion by the smaller Y^{3+} ion, decrease much more significantly the φ angle in $Eu_{0.8}Y_{0.2}MnO_3$. This larger reduction of φ yields in fact a remarkable enhancement of the nearest-neighbor ferromagnetic interactions against the second-neighbor antiferromagnetic ones, which is ascertained by the negative shift of the MnO_6 octahedra symmetric stretching mode eigenfrequency relative to its normal anharmonic behavior [23].

Table II Bond length and bond angle of some selected chemical bonds in $Eu_{0.8}Y_{0.2}MnO_3$.

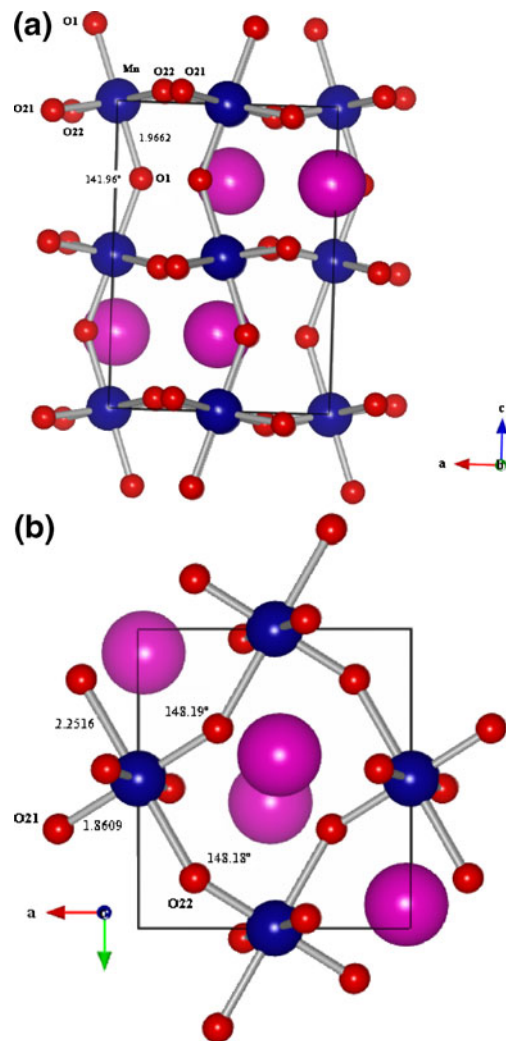| Bond	Distance (Å)	Bond	Angle(º)
Eu/Y – O1	2.3731	O21 – Mn – O22	88.362
	2.2461	Mn – O1 – Mn	141.956
Eu/Y – O21	2.3781	Mn – O22 – Mn	148.188
Eu/Y – O22	2.4965	O1 – Mn – O21	85.852
Eu/Y – O21	2.6180	O1 – Mn – O22	82.773
Eu/Y – O22	3.6135		
Mn – O1	1.9662		
Mn – O21	1.8609		
Mn – O22	2.2516		

Fig. 2 The ac (**a**) and ab (**b**) projections of the unit cell of $Eu_{0.8}Y_{0.2}MnO_3$ at room temperature. The bond lengths are expressed in angstroms

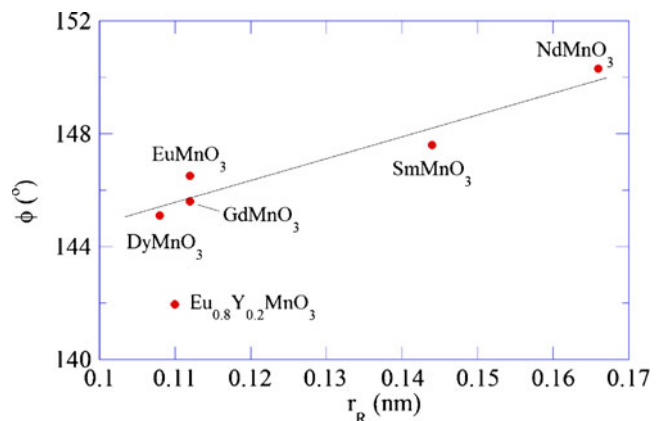**Fig. 3** Mn-O1-Mn angle as a function of the ionic radius of the A-site ion, for the $RMnO_3$, with R = Nd, Sm, Eu, Gd, Dy, and for $Eu_{0.8}Y_{0.2}MnO_3$

$Eu_{0.8}Y_{0.2}MnO_3$ exhibits ferroelectricity in a non-modulated antiferromagnetic phase, pointing out that the ferroelectric properties may have a different origin, different from the one predicted by Dzyaloshinskii-Morya model [14, 23]. Other structural parameters associated with lattice distortions evidence that the Y^{3+} distribution in the crystal lattice enhances structural deformations, which might be associated with the microsocpic mechanisms underlying magnetoelectricity in this compound. Table III exhibits the distortional ratio (τ), the Jahn-Teller parameter (JT), the MnO_6 octahedron distortion parameter (δ), and the average apical compression (ε) for both $EuMnO_3$ and $Eu_{0.8}Y_{0.2}MnO_3$. The mathematical expressions of each parameter are defined in Ref. 24. A pronounced Jahn-Teller distortion is clearly evidenced in $Eu_{0.8}Y_{0.2}MnO_3$, which manifests itself by rather high values of both δ and ε parameters, in fact higher than the ones obtained for undoped $EuMnO_3$.

Scanning electron microscopy (SEM) images of a thermally-etched polished cross-section of the sample were used for ceramographic analysis, as well as for standard quantitative stereology methods, following the grounds of the Heyn method [25]. A typical SEM image is shown in Fig. 4, and it reveals a typical ceramic microstructure, with a rather high degree of compacity and regular shaped crystal grains. Well polished grains do not show any anomalous features, thus assertaining that the sample has an uniform composition. A kind of an one-dimentional growth is observed surrounding grain boundaries, suggesting that during sinterization a small portion of liquid phase is also formed. Further experimental work is needed to clarify this issue. The application of the Heyn method, following the procedure from J. C. Russ[25] to the SEM images yields a grain size number of 11.4. The grain size ranges from 3 μm to 10 μm in diameter.

3.2 Specific heat

Figure 5(a) shows the specific heat C_p/T of $Eu_{0.8}Y_{0.2}MnO_3$ ceramics as a function of temperature. The values of C_p/T are in good agreement with those reported in Ref. 11 for single crystals, corroborating the required stoichiometric

Table III Distortional ratio (τ), Jahn-Teller parameter (JT), MnO_6 octahedron distortion parameter (δ) and average apical compression calculated from the Rietveld analysis of the powder x-ray diffraction spectra of $EuMnO_3$ and $Eu_{0.8}Y_{0.2}MnO_3$. The mathematical expression for each parameter is defined in Ref. 24.

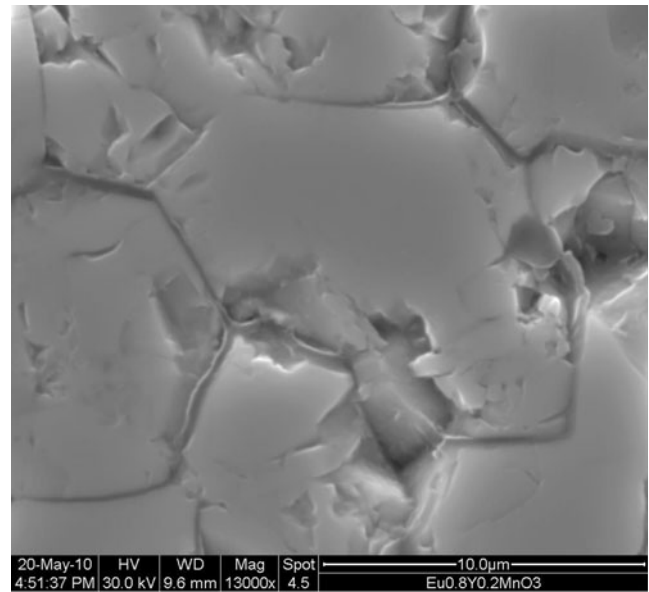|	$EuMnO_3$	$Eu_{0.8}Y_{0.2}MnO_3$
Distortional ratio (τ)	0.161	0.180
Jahn-Teller parameter (JT)	0.0146	0.0161
MnO_6 octahedron distortion parameter (δ)	0.0052	0.0063
Average apical compression	0.0651	0.0682

Fig. 4 Scanning electron microscopic photography of the morphology of the surface of $Eu_{0.8}Y_{0.2}MnO_3$

chemical composition. Two anomalies are clearly observed at T_N=47 K and at T_{AFM-2}~27 K, respectively. According to the phase diagram reported in Ref. 11, the well defined lambda like anomaly at T_N has to be assigned to the
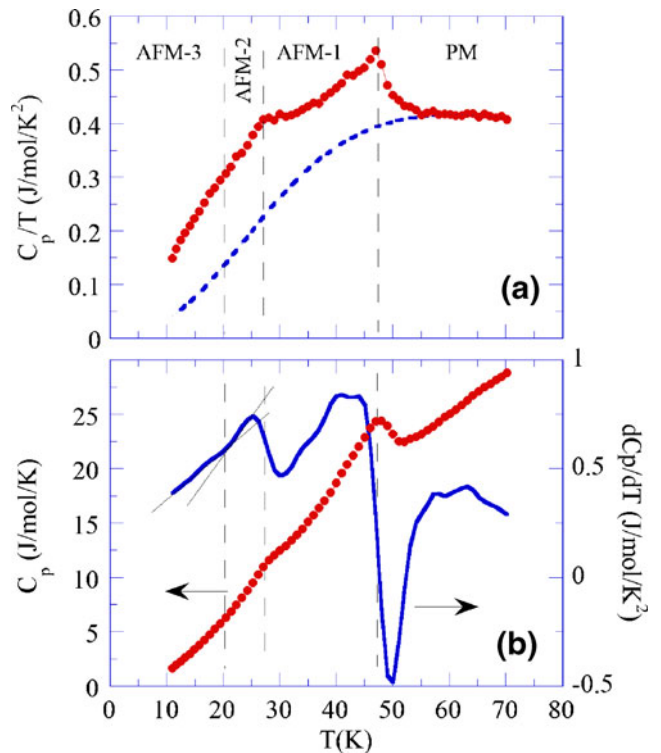

Fig. 5 **a**) Specific heat divided by temperature, as a function of the temperature. The dashed curve presented shows the non-magnetic contribution to the specific heat, obtained from the best fit of the Debye model to the experimental data above 55 K. **b**) Specific heat and its temperature derivative, as a function of the temperatures. The vertical dashed lines signalize the phase transition temperatures

paramagnetic (PM)-incommensurate antiferromagnetic (AFM-1 phase) phase transition, while T_{AFM-2} corresponds to the transition into the non-modulated magnetic AFM-2 phase [13]. The temperatures for the PM/AFM-1 and for the AFM-1/AFM-2 phase transitions agree very well with the results obtained in single crystals. The AFM-2/AFM-3 phase transition could not be seen in the specific heat in agreement with previous work [11]. However, its derivative shown in Fig. 5(b), reveals a small change of slope near 22 K, which is consistent with a transition revealed by other experimental techniques, as it will be described in the next sections. As the measurement of the specific heat does not exceed 80 K, we should expect $C_v \approx C_p$ within the accuracy of the experimental technique.

The high temperature data was analysed by fitting the Debye term, owing to the lattice contribution to the specific heat:[26]

$$C = A\left(\frac{T}{\theta_D}\right)^3 \int_0^{\frac{T}{\theta_D}} \frac{x^4 e^x}{(e^x - 1)^2} dx \qquad (1)$$

In Eq. 1, A is scaling constant, and θ_D is the Debye temperature. In this model, the Debye temperature and the A constant are fitting parameters. The result of the fitting procedure is represented by the dashed line of in Fig. 5(a). The excess of specific heat above this line is due to the magnetic interactions associated with the low temperature magnetic phases. The Debye temperature calculated from the fitting procedure, $\theta_D \approx 210$ K, is in good agreement with the value obtained from the study of active Raman modes in this material [24].

3.3 Dielectric characterization

The temperature dependence of the real (ε'_r) and the imaginary (ε''_r) parts of the dielectric constant, measured at several fixed frequencies, is shown in Figs. 6(a) and (b), respectively. $\varepsilon'_r(T)$ agrees very well with $\varepsilon_a(T)$, reported by Noda et al[12], and Ivanov et al. [24] As the ε_a values are the higher ones found in single crystals, it is expected that the results obtained in ceramic samples are dominated by the dielectric response along the a-axis. A well defined anomaly in $\varepsilon'_r(T)$ and $\varepsilon''_r(T)$ is observed at $T_{AFM-2} \approx 27$ K, corresponding to the transition into the magnetically ordered AFM-2 phase. The maximum variation of ε'_r occurring at T_{AFM-2} is about 1.2, which has nearly the same value of the variation of $\varepsilon_a(T)$ observed by Ivanov et al [27].

The PM/AFM-1 phase transition is signalized by a faint anomaly at $T_N = 47$ K, observed in the detail of $\varepsilon'_r(T)$ curve, depicted in Fig. 6(c). The critical temperature of the AFM-2/AFM-3 phase transition, which occurs close to 22 K [11], can be directly obtained from the analysis of $\varepsilon''_r(T)$ curve (see Fig. 6(c)).

We have analyzed in detail the temperature dependence of $\varepsilon'_r(T)$. The $1/\varepsilon'_r(T)$ does not follows a simple Curie-Weiss
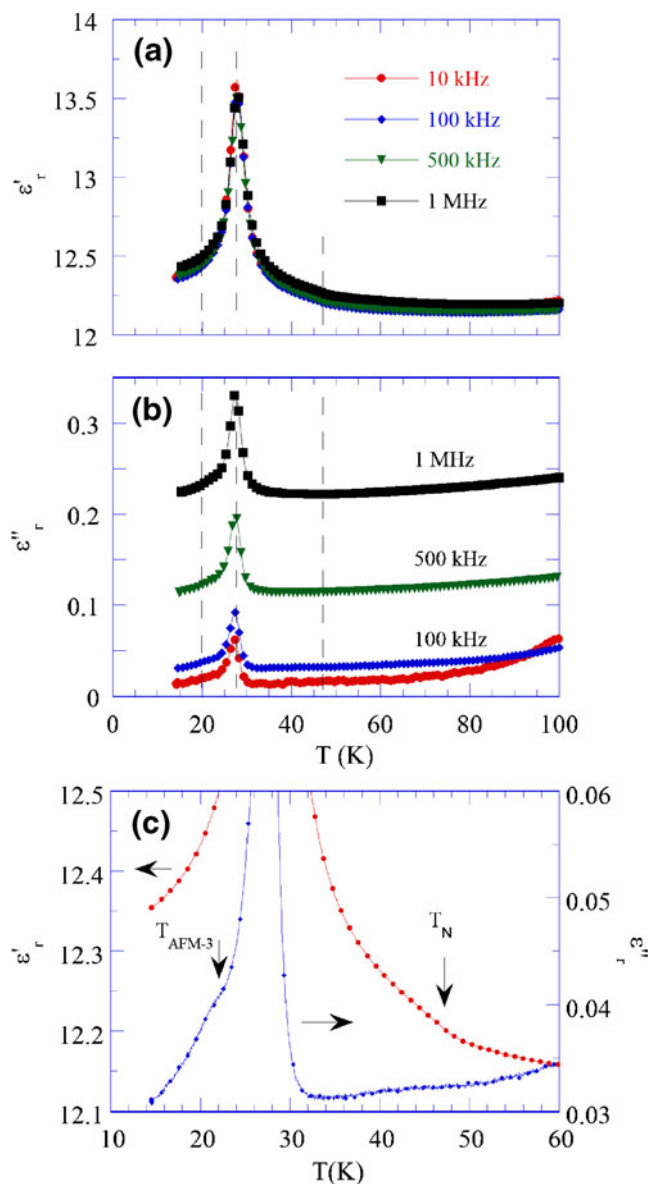

Fig. 6 The temperature dependence of the real (**a**) and the imaginary (**b**) parts of the dielectric constant, measured at several fixed frequencies. (**c**) Detail of the temperature dependence of both real and imaginary parts of the dielectric constant, measured at 100 kHz

law, suggesting that the ferroelectric phase established in the AFM-2 phase does not exhibit a proper character. However, in the particular case of $Eu_{0.8}Y_{0.2}MnO_3$, ferroelectricity does not apparently stem from the well-known Dzyaloshinskii-Morya model [14]. In fact, lattice distortions provided by the Y^{3+} distribution in the crystal lattice may yield the microscopic mechanisms, where magnetoelectricity comes from. Likely though, our results provide evidence for the specific role, played by the MnO_6 Y^{3+}-induced distortions, towards the electronic orbital overlapping, and thus to the magnetoelectric effect itself.

Thermal hysteresis has been detected in $\varepsilon''_r(T)$ below T_{AFM-2}, as we can see in Fig. 7. A strong frequency
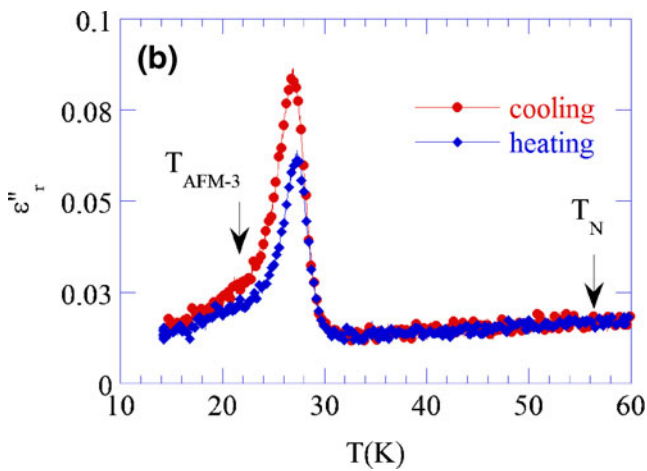
Fig. 7 The temperature dependence of the imaginary part of the dielectric constant, measured at 100 kHz, in cooling and heating runs
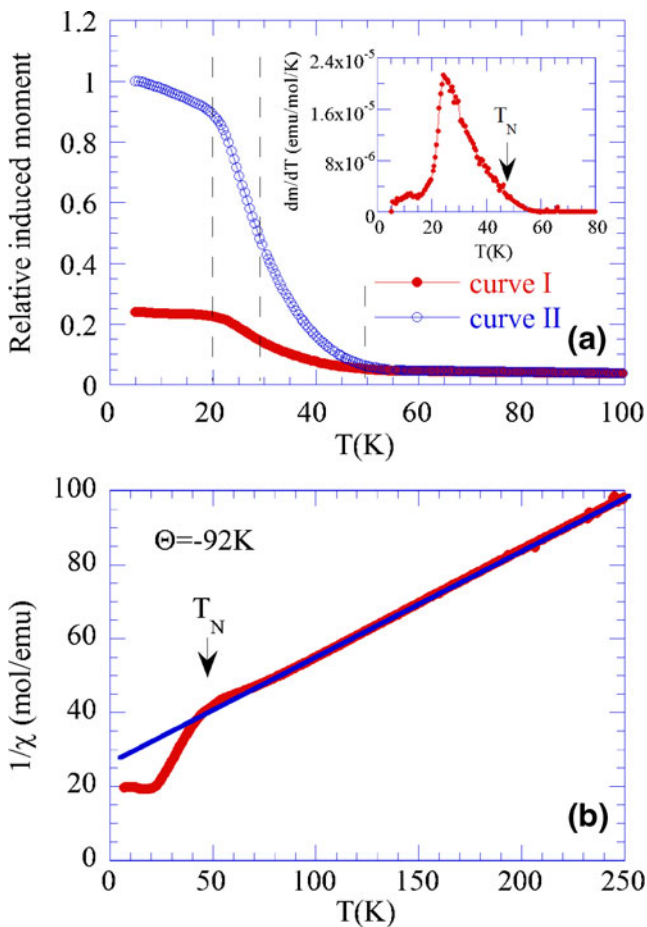

Fig. 8 (a) Temperature behaviour of the induced molar magnetization measured under an applied dc magnetic field of 20 Oe heating the sample after zero field cooling [*curve (I)*], and field-cooling with 20 Oe [*curve (II)*]. Inset of Fig. 7(**a**): temperature derivative of curve (I). (**b**) Temperature dependence of H/M. The solid line was obtained from the best fit of the Curie-Weiss law above T_N
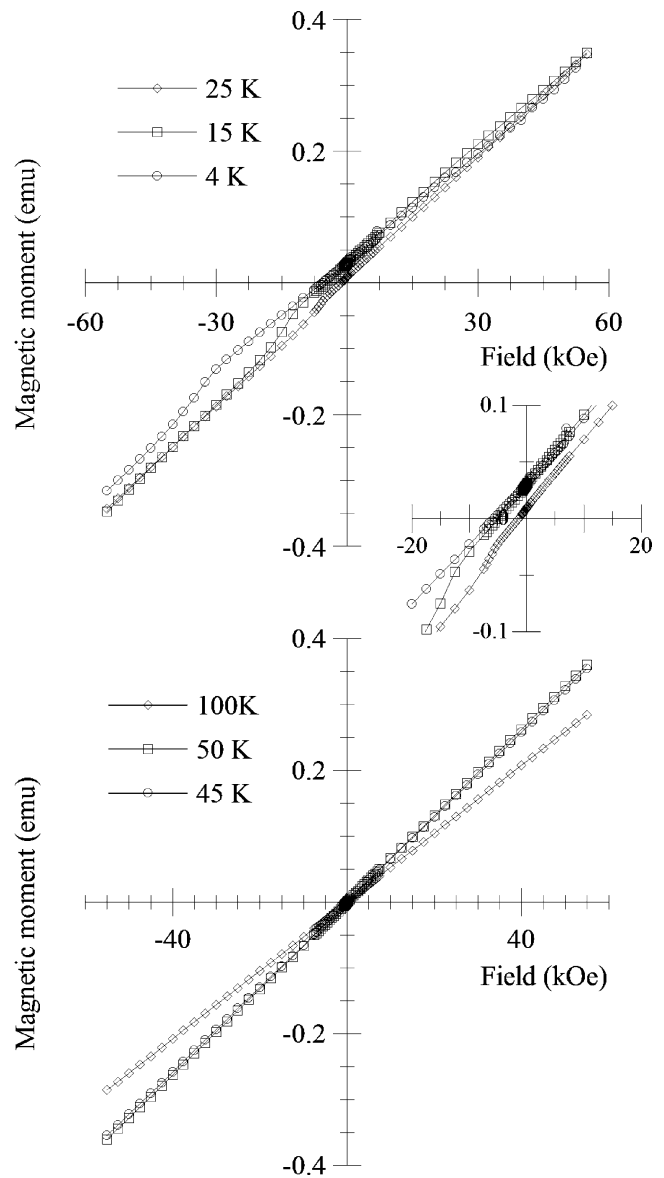

Fig. 9 M(H) relations recorded at several fixed temperatures

dependence of the ε''_r is detected in all temperature range studied. However, contrarily to $EuMnO_3$,[28] it is not observed a relaxation behaviour in the frequency dependence of ε'_r, and no broad anomaly above 40 K can be detected in $\varepsilon''_r(T)$ [11].

3.4 Magnetic characterization

Figure 8a shows the temperature behaviour of the relative induced magnetization measured under an applied dc magnetic field of 20 Oe heating the sample after zero field cooling [curve (I)], and field-cooling with 20 Oe [curve (II)]. The inset of Fig. 8(a) depicts the temperature derivative of curve (I).

As the temperature decreases from 100 K, the induced molar magnetization increases very slowly. At T_N, the

induced magnetization suddenly increases, due to the transition to the AFM-1 phase. At around T_{AFM-3}=25 K, the temperature rate of the induced magnetization reaches its maximum value, as it is clearly observed from the inset of Fig. 8(a). On further cooling, the induced magnetization slightly increases, reaching a plateau below 20 K.

Below T_N, we observed that the induced magnetization is strongly dependent on how the sample is cooled. In fact, upon cooling the sample under an external magnetic field of 20 Oe, significant deviations of both curves are evidenced, reaching a 76% difference at 5 K, which is typically associated with disorder in the magnetic structure, emerging from competitive interactions of FM and AFM generally observed in systems, whose phase diagrams are characterized by existing incommensurate-commensurate superstructures. The increase of the induced magnetization below 40 K is consistent with a ferromagnetic character of the low temperature magnetic phases of this compound, as reported by other authors for single crystals [11, 13]. We have confirmed this result, measuring the M(H) for several fixed temperatures below 100 K, presented in Fig. 9. As the measurements of M(H) using SQUID magnetometer require long time acquisition data (about 36 h each complete M(H)), and as it is usually carried out, we present only a half of M(H) curves, whose shape clearly exhibits the non-linear behaviour associated with the ferromagnetic domain inversion observed below 25 K. As we can see in Fig. 9, the remnant magnetization increases from 9×10^{-3} emu to 3×10^{-2} emu, when the temperature decreases from 25 K to 4 K.

Figure 8(b) shows the temperature dependence of H/M, which exhibits a Curie-Weiss law above 100 K, with a Curie temperature of θ_p=-92±1 K. The calculated value of the effective paramagnetic moment is $(5.6\pm0.1)\mu_B$, which is 10% smaller that the experimental effective moment (μ_{eff}=6.2 μ_B) published for single crystals [11]. It is worth to stress that between T_N and 100 K a deviation of the H/M curve from the expected Curie-Weiss law is observed, which is assigned to dynamical fluctuations of the spins. In fact, similar deviations of phonon response between T_N and 100 K were detected from the study of the infrared absorption in the terahertz region of the paramagnetic phase and Raman scattering, which have been associated with the coupling between phonons and the dynamical fluctuations of the magnetic system [23, 29].

4 Conclusion

Orthorhombic $Eu_{0.8}Y_{0.2}MnO_3$ ceramics were synthesized using urea sol-gel combustion method. The structural, thermodynamic, magnetic and dielectric properties of $Eu_{0.8}Y_{0.2}MnO_3$ ceramics were studied and compared with the physical properties of single crystals. The phase

sequence and critical temperatures found are in good agreement with the corresponding values reported for single crystals. This feature evidences that urea sol-gel combustion method is a suitable route for processing high quality rare-earth manganites ceramics.

Though the anisotropy of both dielectric and magnetic properties is missing, ceramic samples of $Eu_{0.8}Y_{0.2}MnO_3$ have enabled us to identify the main physical mechanisms associated with its magnetoelectric properties. In fact, the improper character of the ferroelectricity in the AFM-2 phase was evidenced from the dielectric data analysis. However, due to the absence of a modulated spin arrangement in this compound below T_{AFM-2}, the ferroelectricity does not apparently stem from the Dzyaloshinskii-Morya mechanism. Our structural study provides evidence for the importance of the deformation of the MnO_6 units in enhancing the ferromagnetic interactions over the antiferromagnetic ones.

Moreover, an important contribution of the magnetic fluctuations above T_N was evidenced in the magnetization studies, corroborating the previous results obtained in the study of the lattice dynamics using different experimental techniques.

References

1. W. Eerestein, N.D. Mathur, J.F. Scott, Nature **442**, 759 (2006)
2. H. Schmid, Int J Magn **4**, 337 (1973)
3. N.A. Hill, J Phys Chem B **104**, 6694 (2000)
4. T. Goto, T. Kimura, G. Lawes, A.P. Ramirez, Y. Tokura, Phys Rev Lett **92**, 257201 (2004)
5. T. Kimura, S. Ishihara, H. Shintani, K.T. Takahari, K. Ishizaka, Y. Tokura, Phys Rev B **68**, 060403 (2003)
6. T. Kimura, G. Lawes, T. Goto, Y. Tokura, A.P. Ramirez, Phys Rev B **71**, 224425 (2005)
7. T. Goto, Y. Yamasaki, H. Wataraba, T. Kimura, Y. Tokura, Phys Rev B **72**, 220403 (2005)
8. M. Mostovoy, Phys Rev Lett **96**, 067601 (2006)
9. I.A. Sergienko, E. Dagoto, Phys Rev B **73**, 094434 (2006)
10. H. Katsura, N. Nagosa, A. Balasky, Phys Rev Lett **95**, 057205 (2005)
11. J. Hemberger, F. Schrettle, A. Pimenov, P. Lunkenheimer, VYu Ivanov, A.A. Mikhin, A.M. Balbashov, A. Loidl, Phys Rev B **75**, 035118 (2007)
12. K. Noda, M. Akaki, T. Kikuchi, D. Akahoshi, H. Kuwahara, J Appl Phys **99**, 08S905 (2006)
13. Y. Yamasaki, S. Miyasaka, T. Goto, H. Sagayama, T. Arima, Y. Tokura, Phys Rev B **76**, 184418 (2007)
14. J. Agostinho Moreira, A. Almeida, W.S. Ferreira, M.R. Chaves, S.M.F. Vilela, P.B. Tavares, Phys Condens Matter **22**, 125901 (2010)
15. J.A. Alonso, M.J. Martínez-Lope, M.T. Casais, M.T. Fernández-Díaz, Inorg Chem **39**, 917 (2000)
16. W. Kraus, G. Nolze, PowderCell for Windows, version 2.3, available at http://ccp14.minerals.csiro.au/ccp/web-mirrors/powd cell/av/v1/powder/ecell.html

17. Available at http://www.rietica.org
18. J. Agostinho Moreira, A. Almeida, M.R. Chaves, M.L. Santos, P. P. Alferesams, I. Gregora, Phys Rev B **76**, 174102 (2007)
19. J.L. Ribeiro, L.G. Vieira, I. Tarroso Gomes, J. Agostinho Moreira, A. Almeida, M.R. Chaves, M.L. Santos, P.P. Alferes, J Phys Condens Matter **18**, 7761 (2006)
20. A. Almeida, J. Agostinho Moreira, M.R. Chaves, A. Klöpperpieper, F. Pinto, J Phys Condens Matter **10**, 3035 (1998)
21. C. Magen, P.A. Algarabel, L. Morellon, J.P. Araújo, C. Ritter, M. R. Ibarra, A.M. Pereira, J.B. Sousa, Phys Rev Lett **96**, 167201 (2006)
22. A.M. Glazer, Acta Crystallogr B **28**, 3384 (1972)
23. J. Agostinho Moreira, A. Almeida, W.S. Ferreira, M.R. Chaves, J. Kreisel, S.M.F. Vilela, P.B. Tavares, Phys Rev B **81**, 054447 (2010)
24. N. Imamura, T. Mizoguchi, H. Yamauchi, M. Karppinen, J Solid State Chem **181**, 1195 (2008)
25. J.C. Russ, *Practical Stereology* (Plenum, New York, 1986)
26. N.W. Ashcroft, N.D. Mermin. Solid State Phys. Thomson Learning (1976)
27. VYu Ivanov, A.A. Mukhin, V.D. Travkin, A.S. Prokhorov, A.M. Kadomtseva, YuF Popov, G.P. Vorob'ev, K.I. Kamilov, A.M. Balbashov, J Magn Magn Mater **300**, 130 (2006)
28. W.S. Ferreira, J. Agostinho Moreira, A. Almeida, M.R. Chaves, J.P. Araújo, J.B. Oliveira, J.M. Machado Da Silva, M.A. Sá, T.M. Mendonça, P. Simeão Carvalho, J. Kreisel, J.L. Ribeiro, L.G. Vieira, P.B. Tavares, S. Mendonça, Phys Rev B **79**, 054303 (2009)
29. R. Valdés Aguilar, A.B. Sushkov, C.L. Zhang, Y.J. Choi, S.-W. Cheong, D. Drew, Phys Rev B **76**, 060404(R) (2007)